nature nanotechnology

SUPPLEMENTARY INFORMATION

DOI: 10.1038/NNANO.2013.125

Destructive Extraction of Phospholipids from *E. Coli* Membrane by Graphene Nanosheets

Yusong Tu [1, 2], Min Lv [2], Peng Xiu [3], Huynh Tien [4], Meng Zhang [2], Matteo Castelli [4], Zengrong Liu [1], Qing Huang [2, *], Chunhai Fan[2], Haiping Fang [2], and Ruhong Zhou [3, 4, 5, *]

[1] Institute of Systems Biology, Shanghai University, Shanghai, 200444, China,

[2] Division of Interfacial Water and Division of Physical Biology, Shanghai Institute of Applied Physics, Key Laboratory of Interfacial Physics and Technology, Chinese Academy of Sciences, P.O. Box 800-204, Shanghai 201800, China,

[3] Department of Engineering Mechanics, and Soft Matter Research Center, Zhejiang University, Hangzhou, 310027, China

[4] IBM Thomas J. Watson Research Center, Yorktown Heights, NY 10598,

[5] Department of Chemistry, Columbia University, New York, NY 10027.

[*] E-mail: Huangqing@sinap.ac.cn, or ruhongz@us.ibm.com

Context:

PS1: Details of the Simulation Systems.

Figure S1 presents the details of the simulation systems. Two types of phospholipids, commonly found in gram-negative bacteria, such as *E. coli,* were used in our simulations, palmitoyloleoylphosphatidylethanolamine (POPE) and palmitoyloleoylphosphatidylglycerol (POPG). The outer membrane is modeled with pure POPE lipid molecules, and the inner membrane with 3:1 mixed POPE-POPG lipids, following previous studies (lipopolysaccharides (LPS) in the outer membrane were omitted for simplicity)[1-4]. Two sizes of graphene nanosheets, 4.92 nm×1.99 nm and 5.41 nm×3.69 nm, were simulated for both the outer and inner membranes, resulting in a total of 4 simulation systems. For the small nanosheet, 256 lipids (256 pure POPE for the outer; and 192 POPE and 64 POPG for the inner) were used, and for the large nanosheet, ~340 lipids (340 pure POPE for the outer; and 258 POPE and 86 POPG for the inner) were adopted. All the systems were then solvated in water,

with large enough water boxes to minimize any potential periodic boundary effects (for example, in the larger nanosheet case, 31141 and 29920 water molecules were used for the outer and inner membrane systems, respectively). Since POPG phospholipid is anionic and carries a unit charge, 64 and 86 Na^+ counter-ions were added in the inner membrane case for the small and large nanosheets, respectively, to neutralize the simulation systems. In order to mimic the graphene sheets with stainless steel substrates in some experiments, one carbon atom at the corner of the graphene nanosheets was position restrained. For the "graphene docking" simulations, an even larger graphene nanosheet with a size of 7.62×3.69 nm^2, was used to better demonstrate the lipid extraction phenomenon. We adopted the GROMOS lipid force field (Berger) for POPE and POPG as implemented in the GROMACS software package version 4.5.4[5], which has been validated extensively[6-9]. Graphene force field parameters are the same as in previous studies[10-12], with carbon atoms modeled as uncharged Lennard-Jones particles with a cross-section of σ_{CC} = 3.58 Å and a depth of potential well ε_{CC} = 0.0663 kcal mol^{-1}. The C-C bond lengths of 1.42 Å, C-C-C bending angles of 120°, and C-C-C-C planar dihedral angles, are maintained by harmonic potentials with spring constants of 322.55 kcal mol^{-1} $Å^{-2}$, 53.35 kcal mol^{-1} rad^{-2} and 3.15 kcal mol^{-1}, respectively. These settings can generate a model graphene with flexural rigidity (0.194 nN nm) reasonably close to *ab initio* results (0.238 nN nm) and other model studies (0.11, 0.225 nN nm)[12]. Water is represented by the simple point-charge SPC/E model. We applied periodic boundary conditions in all directions. The NPT ensemble is used, with temperature controlled at 310 K by the velocity-rescale thermostat with a coupling coefficient of τ_T = 0.1 ps, and the pressure at 1 bar by the Berendsen barostat with a coupling coefficient of τ_P = 1 ps. The particle-mesh Ewald method was used to calculate the long-range electrostatic interactions, whereas the vdW interactions were treated with smooth cutoff at a distance of 12 Å. A time step of 2.0 fs was used, and data were collected every 1 ps. After 40 ns initial equilibrations of solvated lipid systems, the graphene nanosheet was introduced into the system, by replacing overlapping water molecules, initially in parallel with the lipid membrane surface and with a vertical distance of ~4.5 nm from the outer and inner membranes. Position restraints were then applied to the graphene nanosheet for 20 ns to allow system re-equilibration, before production runs.

Both the area per lipid and local bilayer thickness were analyzed for the "extracted region", which is defined as a square region on the membrane surface (x-y plane) surrounding the COM of the nanosheet portion that is immerged inside the membrane, with its side-length 0.6 nm longer than that of the nanosheet. Only those phospholipids whose COM falls into this "extracted region" are counted. The area per lipid in the "extracted region" was computed by dividing the total area of the extracted region by the number of phospholipids inside. The local thickness of lipid bilayer was evaluated as the average distance between the corresponding phosphorus (P) atoms in the two leaflets of a bilayer (i.e., P-P distance).

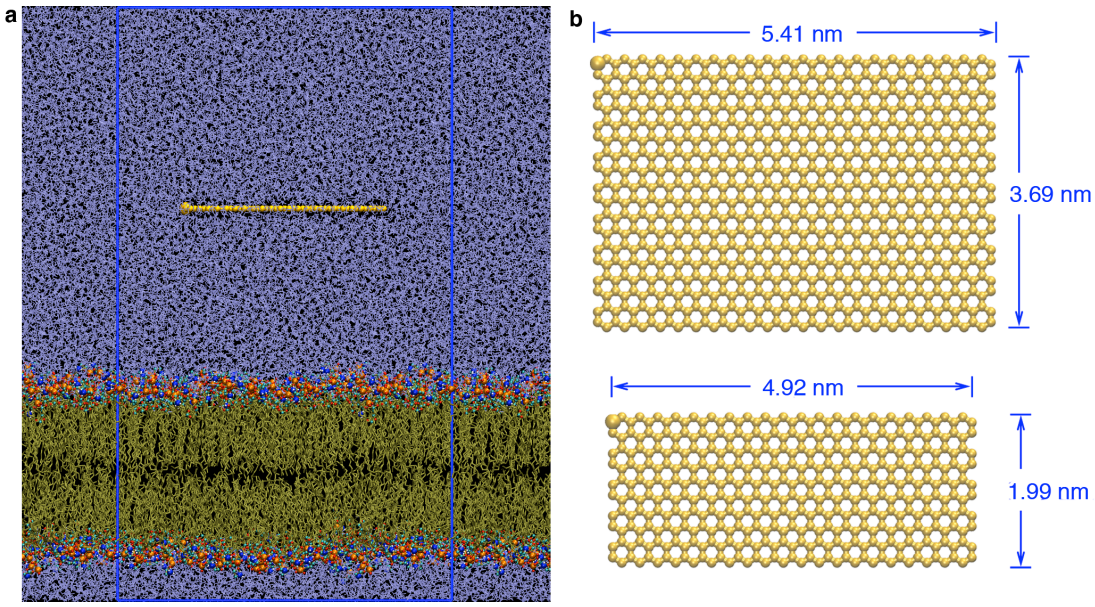

Figure S1. Setup of the simulation systems. The sideview of one example system (the larger nanosheet at the outer membrane) is shown in (a), and dimensions of the two graphene nanosheets (with one large and one small) are shown in (b). Water is shown in ice-blue, and phospholipids in tan lines with hydrophilic charged atoms in colored spheres (hydrogen in white, oxygen in red, nitrogen in blue and phosphorus in orange). In both (a) and (b), graphene atoms are shown in yellow spheres, with a large sphere marked at one corner indicating the restrained atom in simulations. In the "graphene docking" simulations, the graphene sheet with the larger size is further lengthened, with a dimension of 7.62×3.69 nm^2 (not shown).

PS2: Turbulent Phospholipid Extractions after Graphene Insertion.

Figure S2 presents the snapshots of the turbulent lipid extraction by graphene nanosheets once we release the position restraints after their insertion (the "Insertion Mode"). It was shown that the phospholipids were extracted from cell membranes even faster than the restrained cases for both the outer and inner membranes, with several lipids extracted within a few nanoseconds. Also, the inner membrane again displayed slightly faster lipid extraction and stronger graphene attraction.

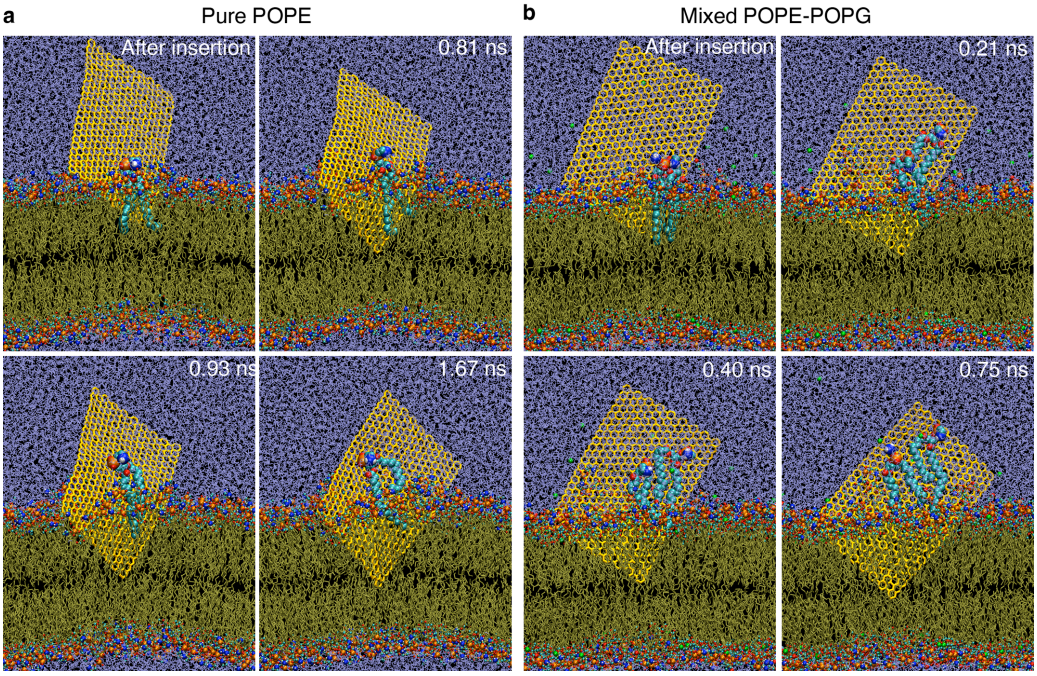

Figure S2. Two representative trajectories for phospholipid extractions by free graphene nanosheets (non-restrained) after their insertion (right after the "Insertion Mode"): (a) the outer membrane (Pure POPE) and (b) the inner membrane (3:1 Mixed POPE-POPG). The phospholipids were extracted from cell membranes extremely fast, within only a few nanoseconds. Again, the inner membrane displayed slightly faster lipid extraction and stronger graphene attraction.

PS3: Instruction to the videos.

The videos Outer_Membrane.swf (**Video S1**), Inner_Membrane.swf (**Video S2**), and Graphene_Docking.swf (**Video S3**) show how graphene nanosheets insert into *E. coli* outer and inner membranes, and how they extract phospholipid molecules directly out of cell membranes. The phospholipids shown in larger spheres are those extracted from their corresponding membranes. Three modes, Swing Mode, Insertion Mode, and Extraction Mode, are highlighted in these videos. Turbulent lipid extractions can be clearly seen in these videos.

Both the outer and inner *E. coli* membranes show a similar behavior, but with the inner membrane displaying slightly faster kinetics and stronger extraction. For example, in the above representative trajectory of the outer membrane (**Video S1**), the graphene nanosheet spent ~140 ns in the Swing Mode, ~15 ns in the Insertion Mode, and then ~30 ns in the Extraction Mode to drag up two POPE molecules. On the other hand, for the inner membrane (**Video S2**), it took ~100 ns in the Swing Mode, ~4 ns in the Insertion Mode, and another ~8 ns in the Extraction Mode to drag up one POPE molecule, followed by ~18 ns to drag up another POPE, and then additional ~25 ns to

drag up one more POPG molecule. In other words, two POPE phospholipids were extracted by the graphene nanosheet in the outer membrane, while three phospholipids (two POPE and one POPG) were extracted from the inner one. After 500 ns simulations, both membranes display significant deformations, with the center of mass (COM) of the outer membrane up 1.60 nm and the inner one up 1.45 nm. Other trajectories with two different sizes of nanosheets show similar results. The slightly faster and stronger extraction of lipids from the inner membrane is probably due to a more favorable full-exposure of charged POPG heads in water than neutral POPE heads[13-15]. However, considering the slightly smaller overall deformation of the inner membrane than the outer one (1.45 nm vs. 1.60 nm in COM movements), the overall interaction strengths of graphene with both membranes are probably comparable.

PS4: Phospholipids tail order parameter in the "extracted regions"

The phospholipid tail order parameter is defined as $S_{cd} = \frac{1}{2}\left\langle 3\cos^2\theta - 1 \right\rangle$, where θ is an instantaneous angle between the nth segmental vector, i.e., (C_{n-1}, C_{n+1}) vector linking $n-1$ and $n+1$ carbon atoms in the acyl chain (here $n = 4-14$) and the bilayer normal; $\langle \mathrm{L} \rangle$ denotes the ensemble average [16]. **Figure S3** shows the average tail order parameters in the "extracted region". As expected, no significant changes to the lipid tail order parameters (i.e., acyl chain orientations).

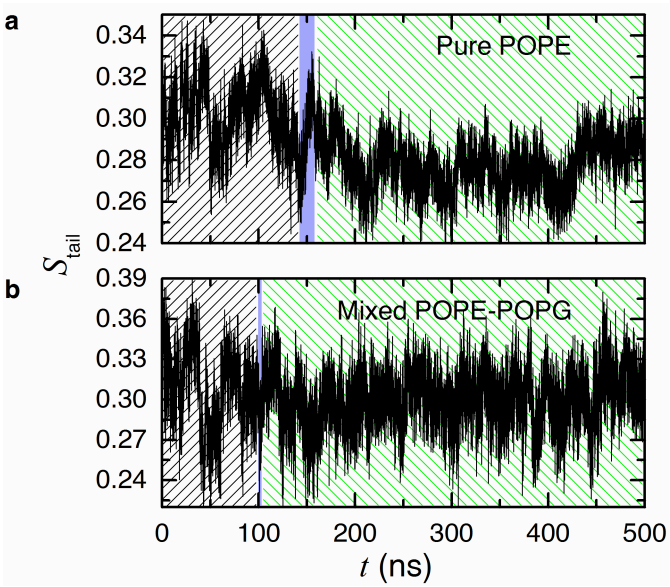

Figure S3. Time evolution of the average tail order parameter in the "extracted region" for the representative trajectories shown in **Fig. 2** (with the top panel for the outer membrane and the bottom panel for the inner membrane). The blue vertical regions indicate the insertion time of the graphene nanosheet in both membranes.

PS5: Extracted phospholipids head orientations

We also examined the structural features of those extracted phospholipids on the graphene nanosheet. A phospholipid includes a hydrophilic head and a hydrophobic tail. Since the hydrophobic tails prefer to stay on the graphene surface, we focused on the orientations of the hydrophilic heads, again using the outer membrane as an example. We found that the head orientations, defined by the angle ϕ_{head} between the graphene surface normal and a vector from the P atom to N atom in a POPE's hydrophilic head (see **Fig. S4** caption for more details), displayed a double-peak distribution. The first peak near $\phi_{head} = \sim 15^\circ$ indicates that those "inner lipids" (near the center of the nanosheet) prefer to have their hydrophilic heads bending into water (see inset in **Fig. S4**), while the second peak at $\phi_{head} = \sim 90^\circ$ suggests that those "edge lipids" favor to have their heads sticking out to water in parallel with the graphene plane.

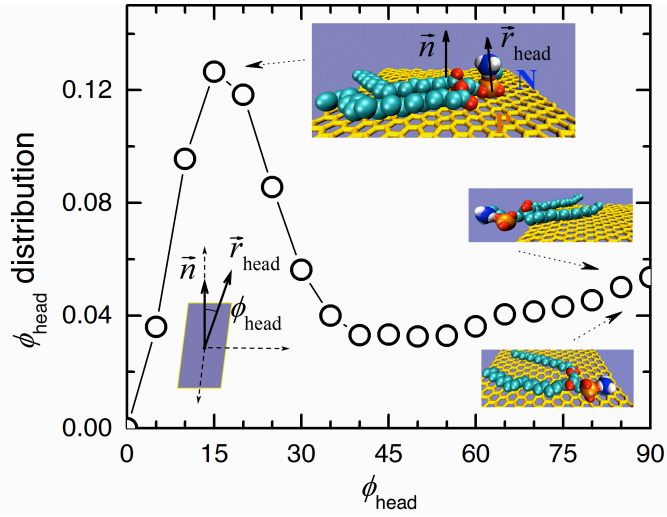

Figure S4. The distribution of the phospholipid heads orientation ϕ_{head} on the graphene nanosheet. The definition of the angle ϕ_{head} is presented at the bottom inset, where $\vec{n}$ is the graphene surface normal, $\vec{r}_{head}$ is the vector from the P atom to N atom in a POPE's hydrophilic head, and ϕ_{head} is the angle between these two vectors. The upper insets present representative structures at the peaks, where the colors of phospholipid atoms are the same as in **Fig. 2**.

PS6: Graphene-oxides with different lateral sizes and concentrations

Different lateral sizes of graphene oxide nanosheets were synthesized according to a modified Hummers method with repeated oxidation, as described in our previous work [17,18]. Atomic force microscopy (AFM) and UV-vis spectra were applied to analyze the properties of GO, and *E. coli* was again used for antibacterial activity

measurements of these GO nanosheets with different lateral sizes and different concentrations.

Figure S5 shows the AFM images of three different types of GO nanosheets, GO1, GO2, and GO3. The thicknesses of the three GO nanosheets are roughly the same, with all approximately 1.1nm, but their lateral sizes are very different. The GO1 nanosheets are polydispersed with a lateral dimension ranging from hundreds of nanometers to micrometers (average size of ~500nm). The average lateral size of GO2 and GO3 was ~200nm and ~50nm, respectively.

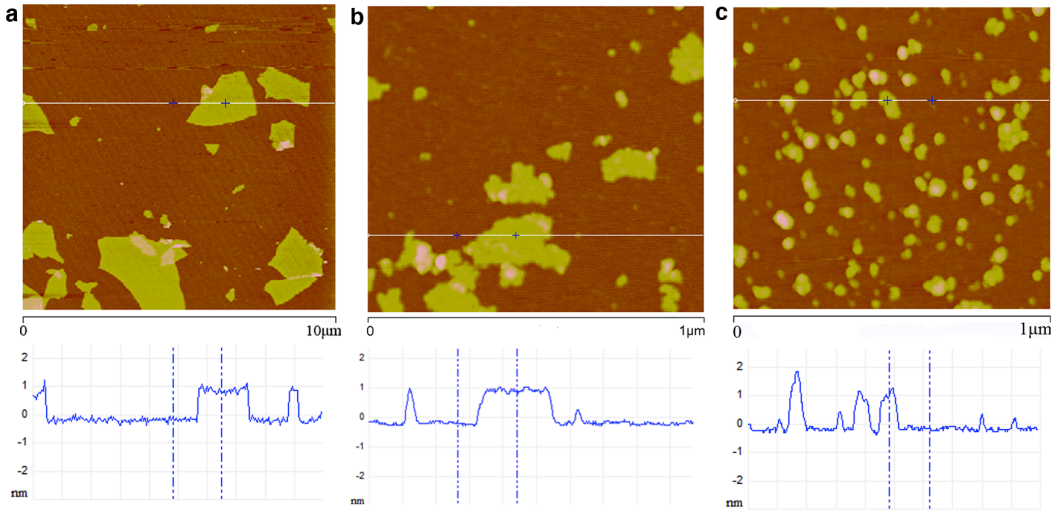

Figure S5. AFM images of three types of graphene oxides nanosheets: GO1 (a), GO2 (b), GO3 (c). The bottom panels show the thickness of the GO nanosheets, which are roughly the same, with all approximately 1.1nm.

Similarly, *E. coli* cells were vaccinated in LB (Luria Bertani broth, Lennox modification) liquid media overnight. The number of $\sim 10^7$CFU/mL *E.coli* cells with suspended graphene oxide nanosheets were cultured at 37°C for 2.5h, and then 100μL bacterial suspension was diluted to 10^6-fold with a gradient method and then coated uniformly on three LB agar plates (with 1.5% agar) per gradient solution. These plates were cultured at 37 °C for 24h. A classic colony counting method was applied to measure the antibacterial activity of graphene oxide. The colony-forming units (CFU) spread on the agar plates were counted and averaged from three replicate tests for each fabric. The antibacterial activity of GO was estimated as follows:

$$\text{Antibacterial Activity (\%)} = \frac{N_{\text{ctrl}} - N_{\text{exp}}}{N_{\text{ctrl}}} \times 100\%$$

where N_{ctrl} is the numbers of bacteria of control, and N_{exp} is the numbers of bacteria of

the experiment group, with different concentrations (20, 50, 100 μg/mL) or different lateral sizes (GO1, GO2 and GO3).

Figure S6 shows that the antibacterial activity of GO is concentration- and lateral-size-dependent. After 2.5h incubation with GO1 nanosheets, the *E. coli* cell death rate increased from 54.3% to 90.9%, when the concentration increased from 25μg/mL to 100μg/mL. This suggests the antibacterial activity of GO nanosheets to *E. coli* increases with GO concentration (**Fig. S6(a)**). On the other hand, with the same 2.5h incubation with 100μg/mL of GO1, GO2, or GO3, their antibacterial activities were 90.9%, 51.8% and 40.1%, respectively (**Fig. S6(b)**), indicating that the antibacterial activity of GO increases with the increase of lateral sizes (GO1 > GO2 > GO3).

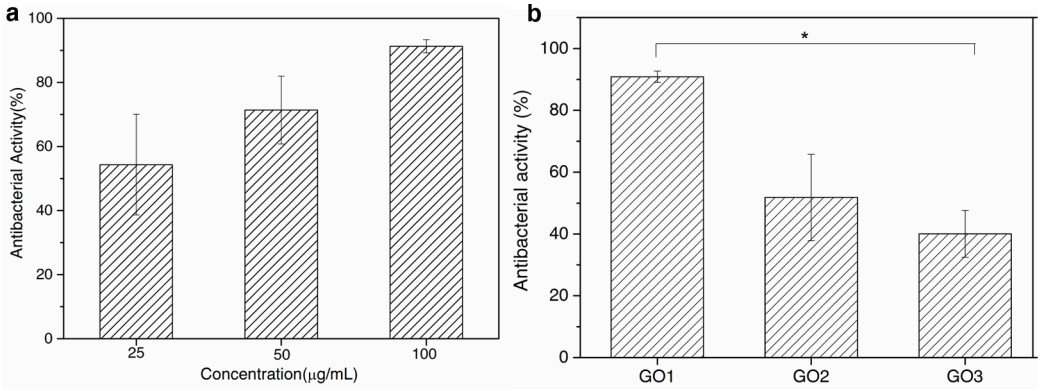

Figure S6. (a) Concentration- and (b) lateral-size-dependent antibacterial activity of GO. (a) *E.coli* was incubated with 25, 50 and 100 μg/mL GO1 at 37°C for 2.5h. (b) *E.coli* was treated with 100μg/mL GO1, GO2 and GO3 at 37°C for 2.5h. (*$p<0.05$).

It was recently proposed that large unoxidized residual graphene-like regions (sp^2-domain) can exist on GO nanosheets [19-21]. We performed UV-vis spectra experiments here to show that the maximum absorption peak of graphene, resulted from sp^2-domain of carbon atoms, would display a blue-shift upon repeated heavy oxidation, such as in the GO3 case, due to the presence of oxygen and increased number of sp^3 bonds. **Figure S7** shows that the maximum absorption peaks of GO1, GO2 and GO3 are at 238, 222 and 218 nm, respectively. With less oxidation (and larger lateral size), this blue-shift is weakened, indicating that there exist larger sp^2-domains with the increase of GO lateral sizes, which result in higher antibacterial activities as shown in **Fig. S6**.

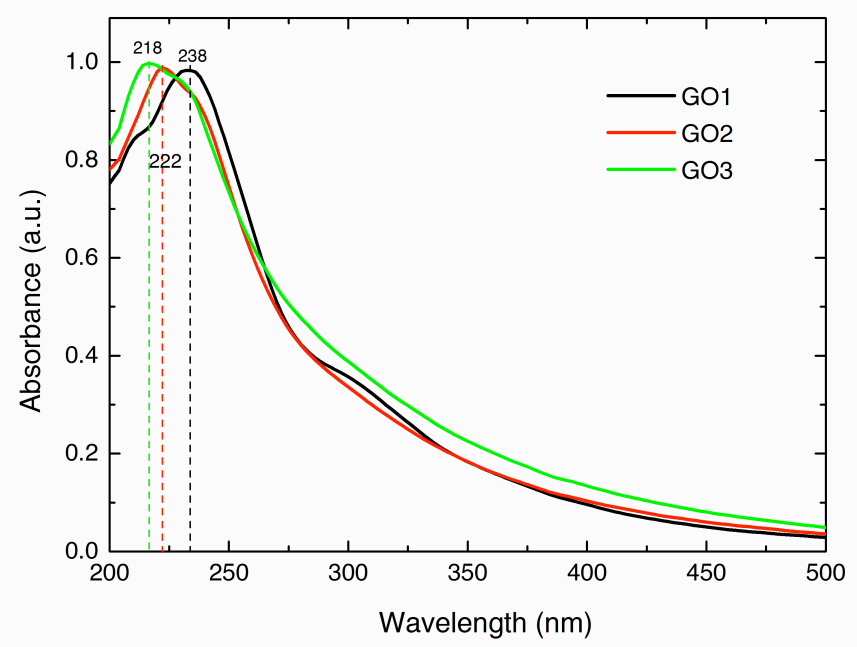

Figure S7. UV-vis absorption spectra of graphene oxides with three different lateral sizes (GO1, GO2, and GO3, same as in **Fig. S5**).

PS7: High correlation between oxidization loci on graphene oxides

To further illustrate the potential existence of large sp^2-domains on GO nanosheets discussed above, we performed quantum mechanics (QM) calculations on the graphene oxidation process and pathways. We analyzed the reaction mechanism of graphene oxidization by permanganate using the Density Functional Theory (DFT) with B3LYP functionals combined with the 6-31G(d) basis set for O, C and H atoms and lanl2dz basis set for Mn atom. Three reaction paths were designed. **Figure S8** presents the relevant geometric structures of the reactants, transition states and products of MnO_4^- oxidizing pure graphene (Path I), graphene with one epoxy (-O-) (Path II), and graphene with one hydroxyl (-OH) (Path III), respectively.

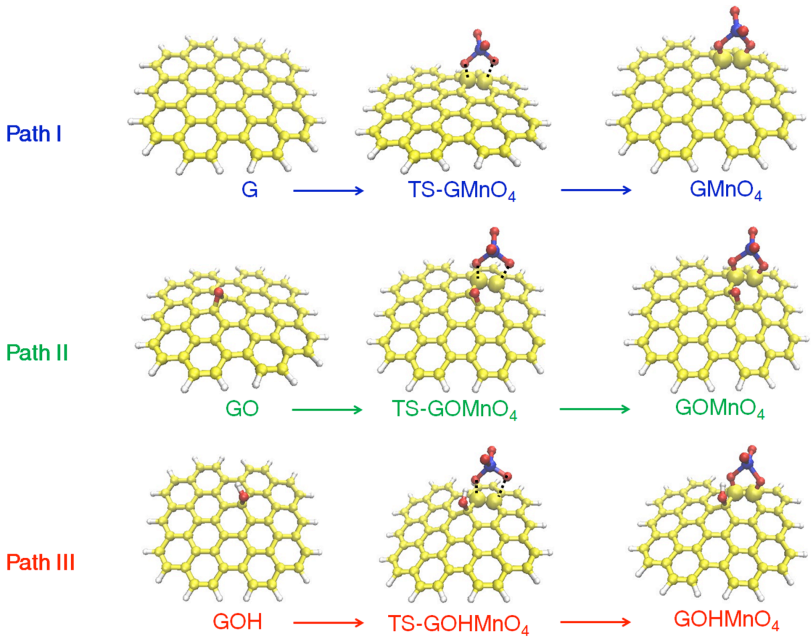

Figure S8. Geometric structures of the reactants, transition states and products of MnO_4^- oxidizing pure graphene (G, TS-$GMnO_4$ and $GMnO_4$ along Path I), graphene with one epoxy (-O-) (GO, TS-$GOMnO_4$ and $GOMnO_4$ along Path II), and graphene with one hydroxyl (-OH) (GOH, TS-$GOHMnO_4$ and $GOHMnO_4$ along Path III).

Figure S9 presents the reaction paths of MnO_4^- oxidizing pure graphene, graphene with one epoxy (-O-) group, and graphene with one hydroxyl (-OH) group. Along Path I, the reaction energy barrier for one carbon atom oxidization on intact graphene by permanganate is 31.9 kcal/mol. Along Path II, the barrier reduces to 24.1 kcal/mol, when one of its neighboring carbon atoms has been pre-oxidized to the -C-O-C- structure. Along Path III, the barrier reduces further to only 17.4 kcal/mol, when one of its neighboring carbon atoms has been pre-oxidized to the C-OH structure.

Furthermore, we applied the conventional transition state theory [22] to analyze the rate constant of the oxidation reaction. The rate constant can be expressed as $k=\kappa\cdot(k_BT/h)(Q_{TS}/Q_R)\exp[-(E_{TS}-E_R)/RT]$, where κ is the tunneling correction, Q_{TS} is the partition function of the transition structure, Q_R is the reactant partition function per unit volume, $(E_{TS} - E_R)$ is the energy barrier, k_B is Boltzmann constant, h is planck constant, R is universal gas constant, and T is the reaction temperature. For simplicity, we estimated the tunneling correction using the Eckwart potential: $\kappa T=1+(h\upsilon^{\neq}/k_BT)^2/24$, where $\upsilon^{\neq}$ is the vibration frequency. The ratio of k_{GO}/k_G between Path II and Path I, and the ratio of k_{GOH}/k_G between Path III and Path I, are 3.95×10^5 and 6.87×10^{11}, respectively.

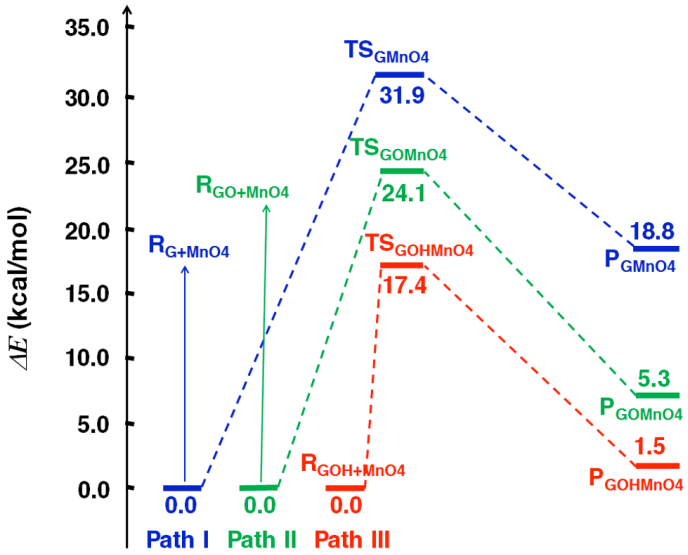

Figure S9. Reaction paths of MnO_4^- oxidizing the pure graphene (Path I), graphene with one epoxy (-O-) group (Path II), and graphene with one hydroxyl (-OH) group (Path III).

These results indicate that one carbon atom on some broken π-bond may be oxidized with much higher probability (once its neighboring atom has been oxidized) than its counterpart with intact π bond. The difference of reaction barrier energy between these two situations can be up to 14.5 kcal/mol, indicating a high correlation between oxidization loci on graphene. This high correlation in oxidization loci explains the recent experimental findings of the isolated highly oxidized areas (few nm in size) and large residual graphene-like sp^2-domains on GO [20,21]. This high correlation between oxidization loci has also been utilized experimentally to achieve the oxidative cutting or unraveling of carbon nanotubes [23].

Finally, it should be noted that although the exact identity and distribution of oxide functional groups is not yet available [24-26], the idea of high correlation of oxidization loci based on our quantum computation coincides with the most popular Lerf-Klinowski model [19], which has been supported by recent experiments with Carbon-13 NMR spectra [27], and XANES and RXE spectra of GO [28]. The Lerf-Klinowski model described GO as a random distribution of oxidized areas bearing the oxygenated functional groups, combined with unoxidized regions wherein most of the carbon atoms preserve sp^2 hybridization. The TEM data also show that upon oxidation isolated highly oxidized areas (few nm in size) are formed while at least ~60% of the surface remains undisturbed [20]. High ratio of unoxidized/oxidized areas are confirmed by other experimental groups as well [21,25,29,30].

Reference

1 Murzyn, K., Róg, T. & Czaplewski, C. Molecular dynamics simulation studies of lipid bilayer systems. *Acta Biochim Pol* **47**, 601-611 (2000).

2 Hallock, K. J. *et al.* Membrane Composition Determines Pardaxin's Mechanism of Lipid Bilayer Disruption. *Biophys J* **83**, 1004-1013 (2002).

3 Lee, S.-Y. & MacKinnon, R. A membrane-access mechanism of ion channel inhibition by voltage sensor toxins from spider venom. *Nature* **430**, 232-235 (2004).

4 Murzyn, K., Róg, T. & Pasenkiewicz-Gierula, M. Phosphatidylethanolamine-Phosphatidylglycerol Bilayer as a Model of the Inner Bacterial Membrane. *Biophys J* **88**, 1091-1103 (2005).

5 Hess, B., Kutzner, C., vanderSpoel, D. & Lindahl, E. GROMACS 4: Algorithms for Highly Efficient, Load-Balanced, and Scalable Molecular Simulation. *J Chem Theory Comput* **4**, 435-447 (2008).

6 Berger, O., Edholm, O. & Jähnig, F. Molecular dynamics simulations of a fluid bilayer of dipalmitoylphosphatidylcholine at full hydration, constant pressure, and constant temperature. *Biophys J* **72**, 2002-2013 (1997).

7 Anézo, C. *et al.* Methodological Issues in Lipid Bilayer Simulations. *J Phys Chem B* **107**, 9424-9433 (2003).

8 Kandt, C., Ash, W. L. & Peter Tieleman, D. Setting up and running molecular dynamics simulations of membrane proteins. *Methods* **41**, 475-488 (2007).

9 Benz, R. W., Castro-Román, F., Tobias, D. J. & White, S. H. Experimental Validation of Molecular Dynamics Simulations of Lipid Bilayers: A New Approach. *Biophys J* **88**, 805-817 (2005).

10 Zuo, G. *et al.* Adsorption of Villin Headpiece onto Graphene, Carbon Nanotube, and C60: Effect of Contacting Surface Curvatures on Binding Affinity. *J Phys Chem C* **115**, 23323-23328 (2011).

11 Titov, A. V., Král, P. & Pearson, R. Sandwiched Graphene−Membrane Superstructures. *ACS Nano* **4**, 229-234 (2009).

12 Patra, N., Wang, B. & Kra l, P. Nanodroplet activated and guided folding of graphene nanostructures. *Nano Lett* **9**, 3766-3771 (2009).

13 Hua, L., Huang, X., Zhou, R. & Berne, B. J. Dynamics of water confined in the interdomain region of a multidomain protein. *J Phys Chem B* **110**, 3704-3711 (2006).

14 Krone, M. G. *et al.* Role of water in mediating the assembly of Alzheimer amyloid-beta Abeta16-22 protofilaments. *J Am Chem Soc* **130**, 11066-11072 (2008).

15 Liu, P., Huang, X., Zhou, R. & Berne, B. J. Observation of a dewetting transition in the collapse of the melittin tetramer. *Nature* **437**, 159-162 (2005).

16 Zhao, W. *et al.* Role of phosphatidylglycerols in the stability of bacterial membranes. *Biochimie* **90**, 930-938 (2008).

17 Hummers, W. S. & Offeman, R. E. Preparation of Graphitic Oxide. *J Am Chem Soc* **80**, 1339-1339 (1958).

18 Zhang, H. *et al.* Uniform Ultrasmall Graphene Oxide Nanosheets with Low Cytotoxicity and High Cellular Uptake. *ACS applied materials & interfaces* **5**, 1761-1767 (2013).

19 Lerf, A., He, H., Forster, M. & Klinowski, J. Structure of Graphite Oxide Revisited ‖ . *J Phys Chem B* **102**, 4477-4482 (1998).

20 Gómez-Navarro, C. *et al.* Atomic Structure of Reduced Graphene Oxide. *Nano Lett* **10**, 1144-1148 (2010).

21 Ganguly, A., Sharma, S., Papakonstantinou, P. & Hamilton, J. Probing the Thermal Deoxygenation of Graphene Oxide Using High-Resolution In Situ X-ray-Based Spectroscopies. *J Phys Chem C* **115**, 17009-17019 (2011).

22 Jeffrey I. Steinfeld, J. S. F., William L. Hase. *Chemical Kinetics and Dynamics*. (Prentice-Hall: Englewood Clitts, NJ, 1989).

23 Kosynkin, D. V. *et al.* Longitudinal unzipping of carbon nanotubes to form graphene nanoribbons. *Nature* **458**, 872-876 (2009).

24 Dreyer, D. R., Park, S., Bielawski, C. W. & Ruoff, R. S. The chemistry of graphene oxide. *Chem Soc Rev* **39**, 228-240 (2010).

25 Chen, D., Feng, H. & Li, J. Graphene Oxide: Preparation, Functionalization, and Electrochemical Applications. *Chem Rev* **112**, 6027-6053 (2012).

26 Kim, H., Abdala, A. A. & Macosko, C. W. Graphene/Polymer Nanocomposites. *Macromolecules* **43**, 6515-6530 (2010).

27 Cai, W. *et al.* Synthesis and Solid-State NMR Structural Characterization of 13C-Labeled Graphite Oxide. *Science* **321**, 1815-1817 (2008).

28 Hunt, A. *et al.* Epoxide Speciation and Functional Group Distribution in Graphene Oxide Paper-Like Materials. *Adv Funct Mater* **22**, 3950-3957 (2012).

29 Mkhoyan, K. A. *et al.* Atomic and electronic structure of graphene-oxide. *Nano Lett* **9**, 1058-1063 (2009).

30 Mattevi, C. *et al.* Evolution of Electrical, Chemical, and Structural Properties of Transparent and Conducting Chemically Derived Graphene Thin Films. *Adv Funct Mater* **19**, 2577-2583 (2009).